nature energy

Article

https://doi.org/10.1038/s41560-025-01912-8

Solvated-intermediate-driven surface transformation of lead halide perovskites

Received: 12 April 2025

Accepted: 17 October 2025

Published online: 21 November 2025

Check for updates

Sanwan Liu[1,2,10], Tianyin Miao[1,10], Jianan Wang[1,10], Yong Zhang[3,10], Rui Chen[1,10], Xia Lei[3], Wenming Qin[4], Zhongjie Zhu[4], Lanlu Lu[4], Zhenhua Chen[5], Peng Cui[6], Liang Li[6], Meicheng Li[6], Erxiang Xu[7], Yang Shen[7], Seong Chan Cho[2], Sang Uck Lee[2], Seong-Ho Cho[2], Zonghao Liu[1,8] ✉, Wei Chen[1,8] ✉ & Nam-Gyu Park[2,9] ✉

The certified quasi-steady-state efficiency of reported inverted perovskite solar cells (PSCs) has rarely surpassed 26%, primarily attributed to interfacial energy-level misalignment and defect-mediated non-radiative recombination. Here we report a surface-phase-transformation strategy of introducing a minuscule amount of *N*-methyl pyrrolidone (NMP) into the piperazinium diiodide (PDI)-dissolved isopropanol solution to mitigate these challenges. We demonstrate that NMP induces a distinct crystallization pathway on perovskite surfaces during the post-treatment stage, transitioning from a solvated intermediate phase to the α-phase perovskite, bypassing the conventional δ-intermediate-phase → α-phase route, which improves the crystallinity of perovskite surfaces and reduces contact losses. Moreover, NMP enhances the interaction between PDI and perovskites, further optimizing interfacial band alignment. Consequently, we demonstrate high certified power conversion efficiencies of 26.87% (stabilized efficiency), 23.00% and 29.08% for single-junction PSCs, mini-modules and all-perovskite tandems, respectively. Maximum-power-point tracking retains 96% of initial efficiency after 2,500 h under 1-sun illumination at 65 °C in ambient air.

Since the pioneering report on stable solid-state perovskite solar cells (PSCs) in 2012[1], perovskite photovoltaics have attracted widespread attention due to their low-cost fabrication, long charge-carrier diffusion lengths and high charge-carrier mobility[2]. Recently, inverted (p–i–n) PSCs have gradually become a research hotspot due to their advantages in power conversion efficiency (PCE), stability, and compatibility with tandem solar cells[3], underscoring their potential for commercialization. Nevertheless, inverted PSCs with certified quasi-steady-state efficiencies exceeding 26% are still rarely reported in the literature. The primary bottleneck lies in the inevitable non-radiative recombination losses, particularly at the perovskite/charge transport layer interface[4–7]. Notably, the development of hole transport materials in recent years has notably mitigated non-radiative recombination losses at the buried interface[8–10], leading to a substantial leap in the performance of inverted PSCs over the past two years. In contrast, non-radiative recombination at the perovskite/electron transport layer (ETL) interface poses a

[1]Wuhan National Laboratory for Optoelectronics (WNLO), Huazhong University of Science and Technology (HUST), Wuhan, China. [2]School of Chemical Engineering, Sungkyunkwan University (SKKU), Suwon, Republic of Korea. [3]Sustainable Energy and Environment Thrust, Function Hub, The Hong Kong University of Science and Technology (Guangzhou), Guangzhou, China. [4]National Facility for Protein Science in Shanghai, Shanghai Advanced Research Institute, Chinese Academy of Sciences, Shanghai, China. [5]Shanghai Synchrotron Radiation Facility (SSRF), Shanghai Advanced Research Institute, Chinese Academy of Sciences, Shanghai, China. [6]State Key Laboratory of Alternate Electrical Power System with Renewable Energy Sources, School of New Energy, North China Electric Power University, Beijing, China. [7]State Key Lab of New Ceramics and Fine Processing, School of Materials Science and Engineering, Tsinghua University, Beijing, China. [8]Optics Valley Laboratory, Hubei, China. [9]SKKU Institute of Energy Science & Technology (SIEST), Sungkyunkwan University, Suwon, Republic of Korea. [10]These authors contributed equally: Sanwan Liu, Tianyin Miao, Jianan Wang, Yong Zhang, Rui Chen. ✉e-mail: liuzonghao@hust.edu.cn; wnlochenwei@hust.edu.cn; npark@skku.edu

more formidable challenge[11], limiting the efficiency of inverted PSCs, as evidenced by a notable reduction in photoluminescence (PL) quantum yield in perovskite/ETL samples[4,7,12]. Although numerous surface passivation strategies have been attempted to address this issue[4,13–16], high-performance inverted PSCs rely on mostly conventional passivation strategies based on ammonium ligands or two-dimensional (2D) perovskite passivation[17–20]. However, ammonium ligands are susceptible to deprotonation under light–thermal stress[6,21], leading to vacancy defects and limiting their passivation effectiveness; similarly, 2D perovskites may also hinder charge transport[22]. Therefore, a more advanced passivation pathway is still required for further exploration.

Here we report a surface-phase-transformation strategy involving crystallization dynamics to minimize non-radiative recombination losses at the perovskite/ETL interface by introducing a minuscule amount of polar aprotic *N*-methyl pyrrolidone (NMP) into a piperazinium diiodide (PDI)-dissolved isopropanol (IPA) solution. We demonstrate that NMP has a prominent role in a distinct crystallization pathway on the ultrathin perovskite surface during the post-treatment process, enabling a transition from a solvated intermediate phase to the α-phase perovskite, bypassing the conventional δ-intermediate phase → α-phase route, which notably enhanced the crystallinity of perovskite surfaces and reduced contact losses. Furthermore, NMP enhanced the interaction between PDI and the perovskite surface without inducing the formation of 2D perovskites, further optimizing interfacial band alignment and suppressing non-radiative recombination. Consequently, the phase-transition-assisted surface-phase-transformation approach yielded certified PCEs of 26.87% (stabilized efficiency) with a high fill factor of 86.06% for single-junction PSCs, 23.00% for mini-modules (aperture area of 11.09 cm^2) and 29.08% for all-perovskite tandem solar cells. Moreover, our devices maintained 95% and 96% of their initial PCEs after aging for over 1,000 h at 85 °C in an N_2 atmosphere and operating for over 2,500 h at 65 °C under 1-sun-equivalent white-light light-emitting diode (LED) illumination in air, respectively.

Exploring the interplay of passivators and solvents

State-of-the-art inverted PSCs currently employ organic ammonium salts (Supplementary Fig. 1) as surface passivators, including propane-1,3-diammonium iodide ($PDAI_2$), 3-(methylthio)propylamine hydroiodide (3MTPAI), phenethylammonium chloride (PEACl), piperazinium iodide (PI), phenethylammonium iodide (PEAI) and PDI, to address surface defects and mitigate complex interfacial carrier recombination issues[4,6,23]. This effectiveness is attributed to the strong interaction between ammonium groups and the perovskite surface (Supplementary Figs. 2 and 3) and the induced n-type doping on the surface[4]. We first conducted the conventional post-treatment with passivator-bearing IPA solutions (saturated passivator solutions) and investigated the dependence of photovoltaic performance on passivators. The current–voltage characteristics of the devices indicate that post-treatment improved PCEs compared with the control devices (without passivation). Among the treated samples, the PDI-treated device exhibited the greatest enhancement in PCE (Fig. 1), probably due to its highest binding energy to the perovskite surface (Supplementary Fig. 3). The average device efficiency was enhanced from 24.80% to 25.49%, achieving a level roughly comparable to most previously reported high-efficiency inverted PSCs based on normal-bandgap perovskites (Supplementary Fig. 4).

However, the low solubility of PDI (Supplementary Fig. 5) in weakly polar IPA (dipole moment = 1.66 D) limits its passivation effectiveness, resulting in the device not fully exhibiting its potential. To address this, we introduced a minute quantity of polar aprotic solvent into the PDI–IPA solution, with a volumetric ratio of polar aprotic solvent to IPA of 1:200. This minuscule amount of polar aprotic solvent is intended to dissolve the ultrathin layer of perovskite films for surface phase transformation (Fig. 1a). We first tried *N*,*N*-dimethylformamide (DMF), a typical parent solvent widely used in perovskite precursors[20,24]. We observed that the DMF-embedded PDI–IPA solution (denoted as PDI–DMF in Fig. 1b) hardly increased the average PCE of devices, probably due to the formation of the δ-phase on the perovskite surface (Supplementary Fig. 6). However, interestingly, the addition of other polar aprotic solvents led to notable enhancement in PCE (Fig. 1b). These solvent systems included IPA–dimethyl sulfoxide (DMSO) (denoted as IPA-D), IPA–diethyl sulfoxide (denoted as DESO), IPA–NMP (IPA-N), IPA–1,3-dimethyl-2-imidazolidinone (denoted as DMI) and IPA–*N*,*N*-dimethylpropyleneurea (denoted as DMPU). The highest average PCE (>26.5%, Fig. 1b; the representative current density–voltage (*J*–*V*) curves of the surface post-treatment strategies involved in Fig. 1b are shown in Supplementary Fig. 7) was achieved with the IPA-N combination. Moreover, scanning electron microscopy images suggest that surface passivation using the polar-aprotic-solvent-embedded PDI enhances the reconstruction effect on the perovskite surface (see IPA-D, IPA-N and DESO cases in Supplementary Fig. 8). The nodules observed in the coordinating-solvent-treated films may originate from the redistribution of PbI_2 on the perovskite surface, induced by the coordinating solvent, thereby exerting a 'shearing' effect on PbI_2 (see details in Supplementary Fig. 9 and Supplementary Note 1). Such redistribution of PbI_2 may also have a role in improving the non-radiative recombination characteristics of perovskite films[25]. This finding was supported by steady-state PL results, where the IPA-N post-treated perovskite film showed the strongest PL intensity (Supplementary Fig. 10). The polar aprotic solvents have been classified into two categories on the basis of their basicity, as defined in terms of Gutmann donor number (DN*, where DN* = DN/38.8) and Kamlet–Taft β values: $\beta \leq$ DN* (DESO, DMPU and DMSO) and $\beta \geq$ DN* (DMI and NMP)[26]. Interestingly, the PL intensity of these perovskite films also follows a distinct trend: for $\beta \leq$ DN*, the PL intensity increases in the following order: IPA-D > DMPU > DESO; for $\beta \geq$ DN*, the PL intensity ranks as IPA-N > DMI. This trend is consistent with the tendency observed in device efficiency in Fig. 1b. Therefore, we focus our further investigation on the two representative cases of IPA-D and IPA-N.

IPA-N characteristics

Grazing-incidence wide-angle X-ray scattering (GIWAXS) measurements at different incidence angles were further performed to characterize the crystallinity of the corresponding perovskite films, both at the surface (Fig. 1c,f,i) (incidence angle of 0.2°; the diffraction intensity data presented in a logarithmic scale are shown in Supplementary Fig. 11) and in bulk (incidence angle of 0.8°) (Supplementary Fig. 12). All GIWAXS scattering results exhibited some degree of local in-plane ordering and a non-uniform distribution along the rings, but no strong texture was observed[27]. The intensity of the (100) crystal plane ($q \approx 1.0$ $Å^{-1}$) on perovskite surfaces is stronger for the NMP- and DMSO-embedded IPA (IPA-N and IPA-D) than for IPA alone (Supplementary Fig. 13). However, within the bulk of the perovskite films, the (100) crystal plane intensity shows no notable difference among the three conditions (Supplementary Fig. 14), indicating that this strategy primarily enhances the crystallinity of perovskite surfaces. Additionally, no 2D perovskite phase was observed in the annealed perovskite films, either on the surface or in the bulk. Notably, time-of-flight secondary ion mass spectrometry results indicate that, in both the IPA and IPA-N cases, PDI primarily remains in the surface region of the perovskite layer (Supplementary Fig. 15).

In situ GIWAXS measurements were further employed to gain deeper insight into the structural evolution of perovskite surfaces during the spinning and annealing processes of post-treatment. The time evolution of GIWAXS spectra during the spinning process for IPA-, IPA-D- and IPA-N-treated perovskite films is shown in Fig. 1d,g,j. The GIWAXS snapshots taken at the end of the spinning process (30 s after spinning) for corresponding cases are shown in Supplementary Fig. 16.

https://doi.org/10.1038/s41560-025-01912-8

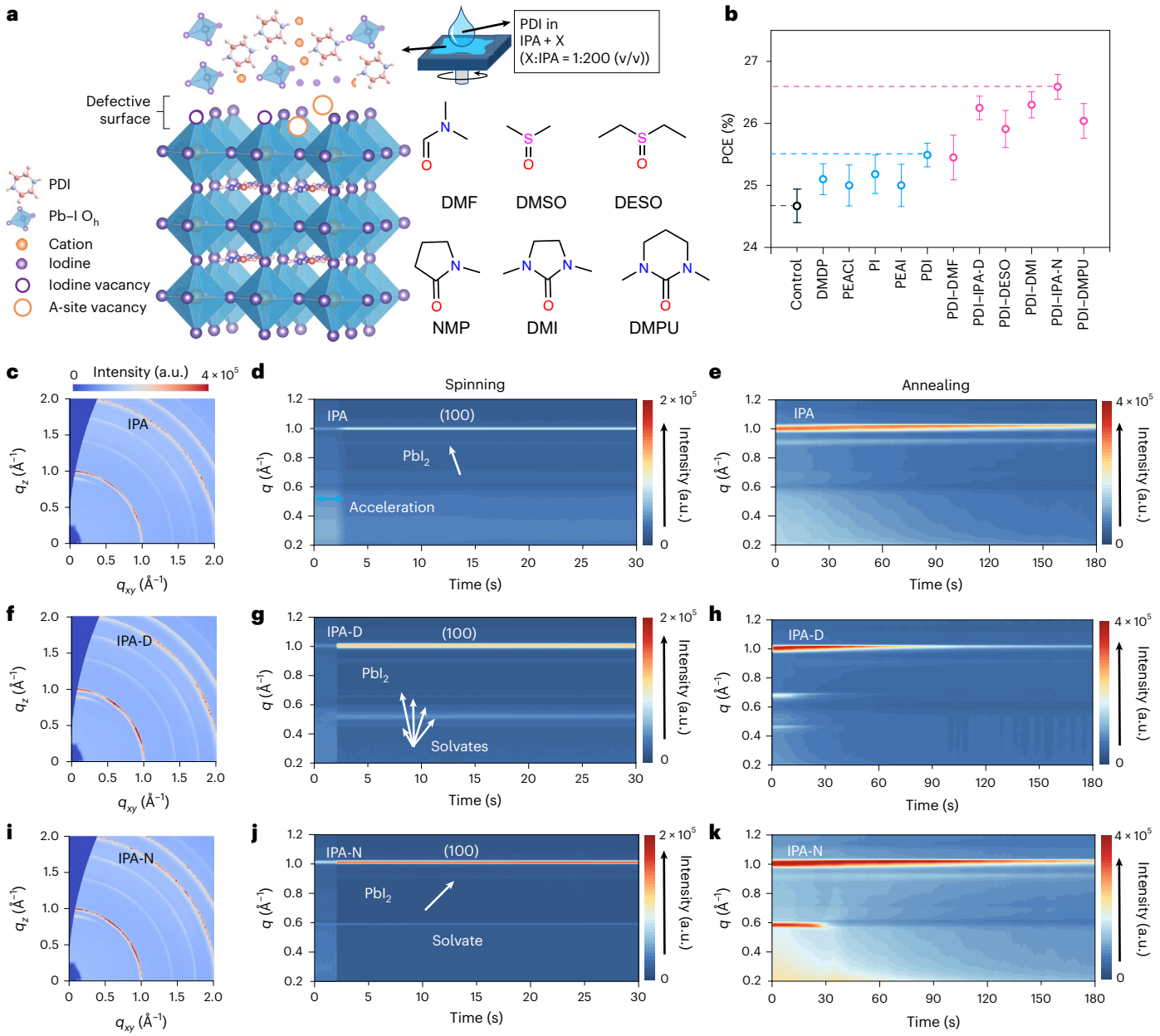

Fig. 1 | The role of IPA-N on perovskite surfaces. a, Schematic illustration of the surface-phase-transformation process via surface passivation using a minute amount of polar aprotic solvent (X) in the PDI-containing IPA solution (X:IPA = 1:200, v/v). The molecular structure of the studied polar aprotic solvents is displayed. **b**, PCEs of the control (black) and passivated PSCs (sky blue and light red). The PCEs are presented as mean ± s.d. from 20 independent devices per condition. Passivation agents include PDI, PEAI, PI, PEACl and DMDP (the binary passivation using $PDAI_2$ and 3MTPAI[4]) dissolved in IPA (sky blue) and X-embedded IPA (light red). Black, blue and light-red dashed lines denote the average efficiencies of control, PDI–IPA- and PDI–IPA-N-treated perovskite devices, respectively. The device efficiencies of control, DMDP, PEACl, PI, PEAI, PDI, PDI–DMF, PDI–IPA-D, PDI–DESO, PDI–DMI, PDI–IPA-N and PDI–DMPU are 24.67% ± 0.27%, 25.10% ± 0.25%, 25.00% ± 0.33%, 25.18% ± 0.31%, 25.00% ± 0.34%, 25.49% ± 0.19%, 25.45% ± 0.36%, 26.25% ± 0.19%, 25.91% ± 0.30%, 26.30% ± 0.21%, 26.59% ± 0.20% and 26.04% ± 0.28%, respectively. **c**,**f**,**i**, 2D GIWAXS patterns of the IPA- (**c**), IPA-D- (**f**) and IPA-N-treated (**i**) perovskite films. **c**,**f**,**i** share a common colour scale bar, which is placed above **c**. a.u., arbitrary units. The incidence angle was 0.2°. q_z and q_{xy} represent the out-of-plane and in-plane scattering vector components, respectively. **d**,**g**,**j**, In situ GIWAXS patterns during the spinning process for the IPA (**d**), IPA-D (**g**) and IPA-N (**j**) cases. Intensity increases upwards along the colour bar, as indicated by the vertical arrow. **e**,**h**,**k**, In situ GIWAXS patterns during the annealing process for the IPA (**e**), IPA-D (**h**) and IPA-N (**k**) cases. Intensity increases upwards along the colour bar, as indicated by the vertical arrow.

The aprotic-solvent-assisted surface treatment did not induce any additional δ-phase formamidinium lead triiodide (δ-$FAPbI_3$) intermediate phase (for example 6H (101)/2H (100)) on the surface[28,29]. Interestingly, multiple weak-scattering rings (peaks) at low q values (≈0.4–0.7 $Å^{-1}$, Supplementary Fig. 17) were observed in the IPA-D case. In contrast, only a single scattering ring at a low q of 0.59 $Å^{-1}$ was observed for the IPA-N case; this was absent from the IPA case without aprotic solvent. These new peaks are ascribed to solvated phases—for example, $FA_2Pb_3I_8$–2DMSO and (FA···NMP) PbI_3 structures[28]. It should be noted that a small amount of NMP (or DMSO) interacts with FA^+ or Pb^{2+} cations through hydrogen bonding or coordination bonding, leading to differences in the energy required for the transition from the corresponding solvent intermediate phase to the α-phase (Supplementary Fig. 18), which is probably the reason for the different solvate phases induced

in the IPA-N and IPA-D cases during the spinning process. In particular, the IPA-treated sample represents a conventional surface passivation approach and does not involve any phase-transition behaviour.

During the annealing process (Fig. 1e,h,k), the corresponding solvated intermediate phases gradually disappear as the annealing time increases for IPA-D and IPA-N cases. The absolute intensities of all the perovskite peaks decreased over time. We speculate that during this in situ treatment PDI gradually coated and accumulated on the surface of the perovskite film as the processing time increased, potentially screening the X-ray scattering from the underlying perovskite film[29]. Therefore, the IPA-N (or IPA-D) cases tuned the crystallization dynamics on perovskite surfaces by inducing solvated intermediate phases during the spinning process. Subsequently, the solvated intermediate phases transformed into the α-phase perovskite during the annealing process, rather than the traditional crystallization pathway (δ-intermediate phase to α-phase) observed in the typical bulk transition[30–32], which is beneficial for reducing stacking defects during the crystallization process and enhancing the crystallization quality of perovskite surfaces[28]. It is important to emphasize that NMP is not the only solvent capable of inducing a positive effect. Other solvents with similar donor numbers can also have a role and exhibit comparable improvements in device performance. Since NMP and DMSO represent two distinct categories of donor-type solvents, we reasonably selected them as representative examples to systematically analyse the unique chemical interactions that different solvents exert on the perovskite surface during the post-treatment process.

The regulation of the crystallization dynamics on the perovskite surface also affects the residual stress at the surface termination. We further investigated the residual stress at perovskite surfaces using the grazing-incidence X-ray diffraction technique with the 2θ–$\sin^2\psi$ method[4] and a penetration depth of 50 nm (Supplementary Note 2). We found that the diffraction peaks of the control and IPA cases gradually shifted to lower 2θ positions on varying ψ from 5° to 45°, while the diffraction peaks of the IPA-N case slightly shifted to higher 2θ positions (Supplementary Fig. 19a–c). The slopes of the fitted lines for the corresponding films by fitting 2θ as a function of $\sin^2\psi$ are shown in Supplementary Fig. 20a. The control and IPA cases exhibited negative slopes, indicating that the films were subjected to tensile stress. In contrast, the slope of the IPA-N case showed a slightly positive value, suggesting favourable compressive stress (Supplementary Fig. 20b). We also conducted grazing-incidence X-ray diffraction analysis based on the (100) plane to further validate the rationale of using the (210) plane for evaluating the film stress (Supplementary Fig. 21). These results indicate that the IPA-N system can release residual tensile stress, which is beneficial for the efficiency and stability of PSCs.

In situ probing of IPA-N passivation dynamics

To reasonably reveal the role of the tailored solvated intermediate phases in defect passivation on the perovskite surface, we further employed in situ PL measurements to monitor the corresponding perovskite films during the spinning and annealing processes. The in situ PL spectra for IPA- and IPA-N-treated perovskite films during the spinning process are shown in Fig. 2a,d. PL intensities increased rapidly for both cases, suggesting a passivation effect of PDI on the perovskite surface. We noted that the PL intensity of the IPA-N-based perovskite film reached its maximum value (2.3×10^4) at 4.4 s, compared with that (1.6×10^4) for the IPA-based film at 3.5 s (Fig. 2c). A slower time to reach the maximum PL with a higher PL intensity observed under the IPA-N condition is indicative of a different passivation pathway compared with the IPA case. A decrease in the PL intensity after reaching its maximum is presumably due to the exposure of the native defective surface during solvent evaporation. Importantly, the passivation effect was more pronounced when PDI was coupled with the IPA-N solvent system, as confirmed by steady-state PL and J–V curves (Supplementary Fig. 22). A strong interaction between PDI and FA^+, as measured using nuclear magnetic resonance (Supplementary Fig. 23 and Supplementary Note 3), is responsible for surface passivation, preventing the deprotonation reaction between A-site cations and suppressing the formation of FA vacancies on perovskite surfaces[33].

During the annealing stage (Fig. 2b,e,f), the PL intensity of IPA-N-based perovskite films reaches its peak faster compared with the IPA condition, indicating that IPA-N exhibits better reactivity with the perovskite surface[34]. Moreover, the maximum PL intensity of the IPA-N-based perovskite film was higher than that for IPA-based films, indicating that the transformation of the solvated intermediate phases into the α-phase under the IPA-N condition could effectively passivate surface defects. Subsequently, the continuous decrease in PL intensity after reaching its maximum intensity for both cases is attributed to the thermal quenching effect of PL[34].

We further compared the suppression effect on iodine vacancies (V_I) at the perovskite surface in both cases using density functional theory (DFT) calculations. The results indicate that the presence of NMP enhances the interaction energy of the original PDI–IPA system with V_I on perovskite surfaces (Supplementary Fig. 24). Moreover, the oxygen atom in NMP has a more negative partial charge ($-0.53\,e^-$) compared with that in IPA ($-0.42\,e^-$), making for stronger hydrogen bonding, as evidenced by the shorter bond length (Fig. 2g). This leads to stronger interaction energy (ΔE_{int}) between NMP and PDI compared with IPA (Supplementary Fig. 25), which explains the more effective defect passivation observed under IPA-N conditions, supported by the time-resolved PL measurements (Supplementary Fig. 26 and Supplementary Table 1). Compared with the control (1.18-μs) and IPA (2.09-μs) cases, the IPA-N case showed a notably longer carrier lifetime (3.91 μs), suggesting that the non-radiative recombination was notably suppressed. In addition, the notably reduced metallic Pb cluster (Pb^0) observed from the X-ray photoelectron spectroscopy (Supplementary Fig. 27 and Supplementary Note 4) suggests a suppressed formation of PbI_2-related degradation products under vacuum[35]. Therefore, the PDI in the IPA-N system can preferably suppress in situ defect-assisted non-radiative recombination by adjusting the crystallization kinetics on perovskite surfaces via the solvated intermediate phase (Fig. 2h, Supplementary Fig. 28 and Supplementary Note 5). Consequently, a high-quality, low-defect perovskite surface is obtained, which is crucial for achieving top-performing PSCs.

Analysis of surface and interfacial losses

We further evaluated the uniformity of perovskite surfaces using laser confocal fluorescence lifetime imaging microscopy. As shown in Fig. 3a–c, the IPA-N system exhibited improved uniformity and enhanced PL lifetimes compared with those of control and IPA cases, indicating that IPA-N improved the uniformity of surface electrical properties, which is crucial for reducing interfacial contact losses. This is particularly important for the fabrication of large-area solar modules.

To further investigate interfacial carrier recombination, we measured the PL quantum yield (PLQY) of the corresponding stacked devices and estimated the quasi-Fermi level splitting using PLQY (Supplementary Note 6). As shown in Fig. 3d and Supplementary Fig. 29, the IPA-N-treated perovskite films exhibited notably enhanced PLQY compared with the control and IPA cases. Notably, after [6,6]-phenyl-C_{61}-butyric acid methyl ester (PCBM) deposition (w/ PCBM), the IPA-N case retained more than 70% of its initial PLQY, whereas the PLQY of the control case decreased notably. This indicates that IPA-N notably reduces interfacial non-radiative recombination, as reflected in the quasi-Fermi level splitting value (Supplementary Figs. 30 and 31 and Supplementary Table 2) for the IPA-N case (1.202 eV), showing a 28-meV enhancement compared with the control case (1.174 eV) under the condition with PCBM.

Ultraviolet photoelectron spectroscopy measurements were used to look into the effect of the IPA-N strategy on the band-edge energies of perovskites (Fig. 3e, Supplementary Fig. 32

https://doi.org/10.1038/s41560-025-01912-8

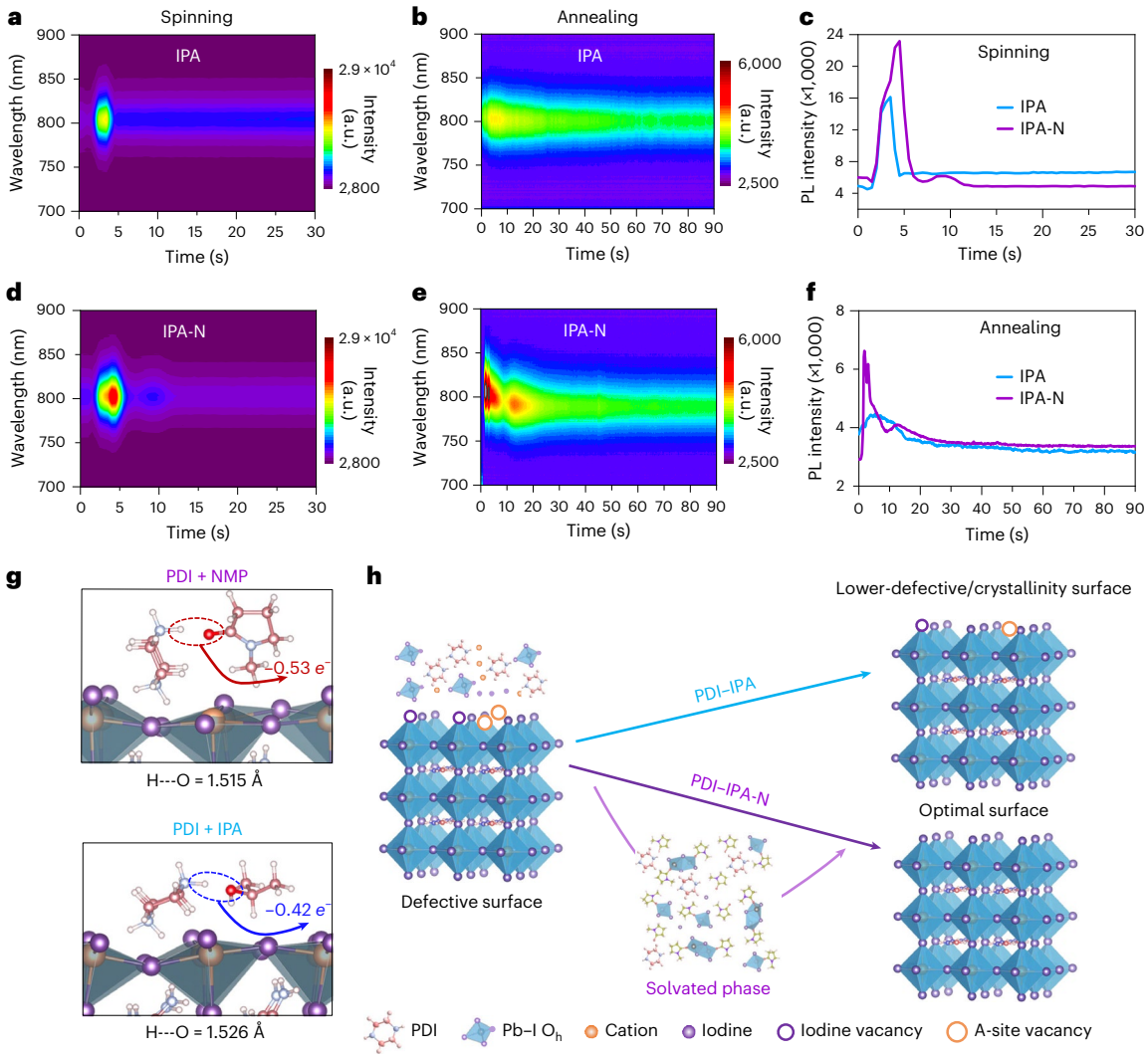

Fig. 2 | In situ probing of IPA-N passivation dynamics. a,**d**, In situ PL spectra during the spinning process for the IPA-treated (**a**) and IPA-N-treated (**d**) perovskite films. **b**,**e**, In situ PL spectra during the annealing process for the IPA-treated (**b**) and IPA-N-treated (**e**) perovskite films. **c**,**f**, In situ PL spectra showing wavelength shift of the maximum peaks of IPA and IPA-N cases during spinning (**c**) and annealing (**f**) processes. **g**, Binding configurations of PDI on NMP@$FAPbI_3$ and IPA@$FAPbI_3$ surfaces, showing hydrogen bonding (H···O) and the Mulliken charge on the O atom of NMP and IPA (the dashed circle means the hydrogen bonds, and the indicated value is the charge on the oxygen). H, C, N, O, I and Pb atoms are represented as white, light-red, light-blue, red, purple and brown spheres, respectively. **h**, Schematic illustration of the mechanism of the IPA-N treatment, showing phase conversion via the solvated intermediate phase on perovskite surfaces.

and Supplementary Table 3). We found that the Fermi level (E_F) on IPA-N treatment shifted closer to the conduction band minimum of the perovskite surface, which is favourable for electron extraction at the perovskite/ETL interface. We also assessed the electron density (η) in the conduction band near the perovskite surface[7] (Fig. 3f and Supplementary Fig. 33). The electron density increased to 3.4×10^{11} cm^{-3} after IPA-N treatment compared with 2.2×10^{7} cm^{-3} and 2.3×10^{9} cm^{-3} for control and IPA cases, respectively, which is attributed to the improved n-type doping effect of the IPA-N system. We further employed femtosecond transient absorption spectroscopy to study the impact of IPA-N treatment on the dynamics of charge extraction at the perovskite/PCBM interface (Fig. 3g–i and Supplementary Fig. 34). Both the control and IPA-N cases exhibited a characteristic ground-state bleaching (GSB) signal at approximately 785 nm. Notably, the IPA-N case (Fig. 3g) showed a faster GSB recovery than the control case (Fig. 3h). Tracking the decay of the GSB at 785 nm revealed that earlier electron extraction was obtained after IPA-N treatment[14] (Fig. 3i and Supplementary Table 4), indicating that the IPA-N system facilitates electron extraction at the perovskite/ETL interface.

Photovoltaic characteristics

Using the IPA-N strategy, we fabricated inverted PSCs with the structure ITO/NiO_x/SAMs/perovskite/PCBM/BCP/Ag, where ITO is indium tin oxide, NiO_x nickel oxide, SAMs self-assembled molecules ([4-(3,6-dimethyl-9H-carbazol-9-yl)butyl]phosphonic acid (Me-4PACz) and 4,4′,4″-nitrilotribenzoicacid (NA) were mixed to use as the SAMs for hole-selective contact)[5,36] and BCP bathocuproine (Supplementary Fig. 35). The photovoltaic parameters of the devices are displayed in Supplementary Figs 36 and 37, and summarized in Supplementary Table 5. The *J*–*V* curves of the champion PSCs for control, IPA and IPA-N devices, along with those for the IPA-D system, are displayed in Supplementary Fig. 38. Obviously, the efficiencies of the devices based on the IPA-N are higher than those of the control and IPA cases, with contributions from the synergistic enhancement of the open-circuit voltage (V_{OC}), short-circuit current density (J_{SC}) and fill factor. The control device yielded a PCE of only 24.97%, with V_{OC} = 1.145 V, J_{SC} = 26.00 mA cm^{-2} and fill factor = 83.86% (steady-state PCE of 24.51% after maximum-power-point tracking (MPPT) for 300 s). Surprisingly, the IPA-N device showed a PCE of 26.80%

https://doi.org/10.1038/s41560-025-01912-8

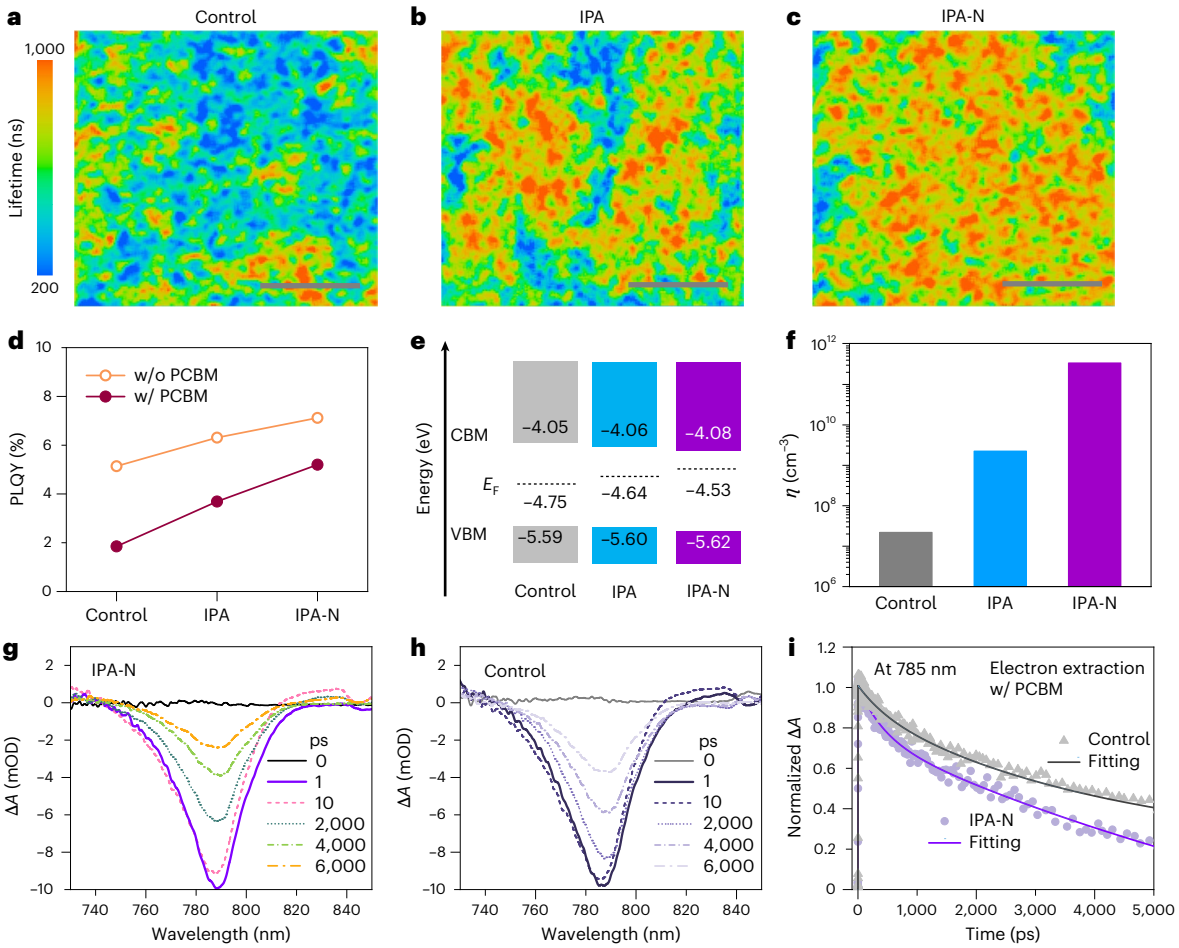

Fig. 3 | Analysis of surface and interfacial losses. a–c, Fluorescence lifetime imaging microscopy of the control (**a**), IPA-treated (**b**) and IPA-N-treated (**c**) perovskite films. Scale bars, 10 µm. **d**, PLQY of the control, IPA-based and IPA-N-based perovskite films with and without PCBM deposition. **e**, Schematic diagram of energy levels of conduction band minimum (CBM) and valence band maximum (VBM), along with E_F, derived from ultraviolet photoelectron spectra. **f**, η in the conduction band near the perovskite surface with different post-treatment methods. **g**,**h**, Femtosecond transient absorption spectra at a selected pump–probe delay time of IPA-N (**g**) and control (**h**) perovskite films with PCBM ETL. **i**, Corresponding GSB decay at 785 nm of the control and IPA-N-treated perovskite films with PCBM ETL. ΔA, difference in optical density between the excited state and the ground state of a sample. Solid lines represent biexponential fits to the experimental data (grey triangles and purple circles), described by $y = A_1 \exp(-t/\tau_1) + A_2 \exp(-t/\tau_2)$, where τ_1 and τ_2 correspond to the fast and slow decay components, respectively. The fitted lifetimes are summarized in Supplementary Table 4.

(steady-state PCE of 26.58%). The external quantum efficiency (EQE) data showed that the integrated J_{SC} of the champion IPA-N device was 25.61 mA cm^{-2} (Supplementary Fig. 39), further confirming that both PDI and NMP are indispensable for enhancing the PCE of the devices (Supplementary Fig. 40). Furthermore, on the basis of the IPA-N strategy and the optimized substrates (fluorine-doped tin oxide substrates from Asahi), we achieved an impressive PCE of up to 27.19% under reverse scan (steady-state PCE of 26.95%) and a fill factor as high as 86.70% (Fig. 4a and Supplementary Table 6). The IPA-N devices were certified by the Chinese National Center of Inspection on Solar Photovoltaic Products Quality, where a PCE of 27.27% with a fill factor of 86.06% from the reverse J–V scan (stabilized PCE of 26.87%) was confirmed (Supplementary Fig. 41). This result is one of the highest certified PCEs among inverted PSCs (Fig. 4b and Supplementary Table 7).

To gain insights into the mechanism of the improved fill factor via the IPA-N approach, we conducted an fill factor loss analysis (Supplementary Note 7 and Supplementary Figs. 42 and 43). The improved fill factor is mainly attributed to reduced non-radiative recombination losses, indicating that defect-assisted trap states were suppressed, which is consistent with the corresponding thermal admittance spectroscopy measurement results (Supplementary Fig. 44), where the IPA-N device exhibited a lower trap density of states[37]. Capacitance–voltage (C–V) characterization was used to explore the separation of photogenerated carriers. The built-in potential (V_{bi}) values were 1.00 V and 1.05 V for the control and IPA-N devices, respectively (Supplementary Fig. 45), which was beneficial for charge separation and transport[38], as further confirmed by the transient photocurrent results (Supplementary Fig. 46).

To further evaluate the upscaling capability of the IPA-N approach, we successfully fabricated top-performing mini-modules with an aperture area of 11.09 cm^2 (Fig. 4c). The mini-module exhibited an impressive PCE of 23.17% (Supplementary Table 8, V_{OC} = 5.93 V, J_{SC} = 4.85 mA cm^{-2} and fill factor = 80.57%) from the reverse scanned J–V curve. A high certified PCE of 23.00% with a fill factor of 80.39% for an IPA-N mini-module was demonstrated by an independently accredited laboratory (Hangzhou branch of TÜV Rheinland Group) (Supplementary Fig. 47). This result represents one of the highest reported certified PCEs for inverted mini-modules (Supplementary Fig. 48 and Supplementary Table 9).

In addition to efficiency, we also considered the impact of the IPA-N method on the stability of perovskite films and devices. Atomic-force-microscopy-based infrared spectroscopy results showed that the IPA-N-treated film exhibited stronger infrared activity

https://doi.org/10.1038/s41560-025-01912-8

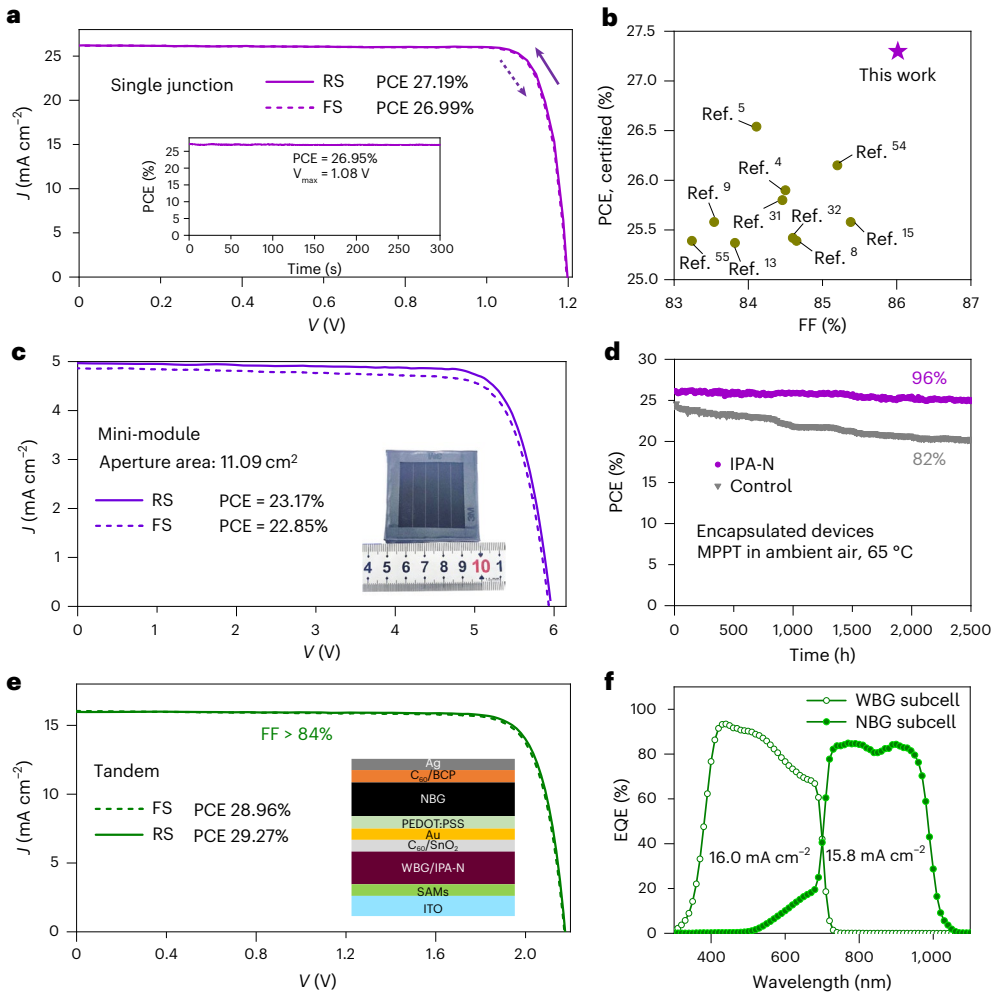

Fig. 4 | Device performance and stability. a, The reverse scanned (RS) and forward scanned (FS) *J*–*V* curves of the champion inverted PSC (single junction) based on the IPA-N method (fabricated on fluorine-doped tin oxide substrates). Inset: the steady-state curve of the device. **b**, Comparison of certified fill factor (FF) and PCE of our device with those of other representative high-performance (PCE > 25%) inverted PSCs reported in the literature[4,5,8,9,13,15,31,32,54,55]. **c**, The RS and FS *J*–*V* curves of the champion mini-module with an aperture area of 11.09 cm^2 based on the IPA-N method. Inset: a photograph of the real device. **d**, Operational stability of encapsulated single-junction devices under continuous 1-sun-equivalent white-light LED illumination with MPPT at 65 °C in ambient air (40 ± 5% relative humidity). The initial PCEs of the representative control and IPA-N devices used for the operational stability test were 24.27% and 26.12%, respectively. **e**, The RS and FS *J*–*V* curves of the champion perovskite/perovskite tandem device. Inset: the device structure with the IPA-N-treated WBG perovskite. **f**, EQE of the perovskite/perovskite tandem solar cells showing EQE corresponding to WBG and narrow-bandgap (NBG) subcells.

at 1,712 cm^{-1} (characteristic vibrational mode of FA) compared with the control case after 500 h of aging at 85 °C in a nitrogen glovebox (Supplementary Fig. 49 and Supplementary Note 8). The weaker activity of FA in the control sample might be attributed to the volatilization of FA and the increased formation of PbI_2 during thermal aging. Furthermore, the aged control sample exhibited a pronounced reduction in the (100) diffraction peak intensity and a substantial increase in the relative intensity of the PbI_2 peak in the XRD pattern (Supplementary Fig. 50a,b). In contrast, the IPA-N-treated film showed only a slight enhancement of the PbI_2 signal, while the (100) peak remained well defined. Consistently, the ultraviolet–visible (UV–vis) absorption spectra revealed a notable shift in the absorption edge of the control film upon aging, whereas the absorption onset of the IPA-N-treated sample remained virtually unchanged (Supplementary Fig. 50c,d). These findings further corroborate that PbI_2 formation is a critical degradation pathway in perovskite films and highlight the effect of IPA-N in mitigating this degradation process. Furthermore, the unencapsulated IPA-N devices retained 95% of the initial PCEs after 1,000 h of thermal aging at 85 °C in a nitrogen atmosphere, whereas the control devices retained only 79% of the initial PCEs (Supplementary Fig. 51). Additionally, after 2,500 h of continuous 1-sun illumination under MPPT at 65 °C in ambient air, the encapsulated IPA-N-based device maintained 96% of its initial PCE, while the control device decreased to 82% of its initial PCE (Fig. 4d and Supplementary Figs. 52 and 53). Moreover, the IPA-N-treated device retained 95% of its initial PCE after continuous 1-sun illumination under MPPT for 732 h at 85 °C (Supplementary Fig. 54).

To explore the applicability of the IPA-N approach to other perovskite compositions, we fabricated wide-bandgap (WBG) PSCs with different bandgaps. Specifically, WBG devices based on perovskite compositions of $FA_{0.8}Cs_{0.2}Pb(I_{0.8}Br_{0.2})_3$ (bandgap of 1.68 eV) and $FA_{0.8}Cs_{0.2}Pb(I_{0.6}Br_{0.4})_3$ (bandgap of 1.77 eV) achieved PCEs of 22.92% (FF of 84.60%) (Supplementary Fig. 55) and 21.15% (FF of 84.88%) (Supplementary Fig. 56), respectively. It should be noted that the IPA-N strategy also exhibits certain positive effects in Sn–Pb mixed perovskite compositions, although its impact is relatively limited (Supplementary Fig. 57). Furthermore, using the 1.77-eV WBG perovskite composition treated with IPA-N, we fabricated all-perovskite tandem solar cells (Supplementary Fig. 58). The champion tandem device (Fig. 4e and Supplementary Table 10) yielded an impressive PCE of 29.27% with a high fill factor of 84.19%. The EQE spectra

showed well-matched current responses (Fig. 4f). It is worth noting that the IPA-N-based all-perovskite tandem solar cells achieved a certified PCE of 29.08% (Supplementary Fig. 59) from an independently accredited institution (Shanghai Institute of Microsystem and Information Technology), which is among the highest certified PCEs reported for perovskite/perovskite tandem solar cells to date (Supplementary Fig. 60 and Supplementary Table 11). Our results confirm that the phase-transition-assisted surface phase transformation approach based on the IPA-N system is applicable across various device architectures, including single-junction inverted devices, mini-modules and all-perovskite tandem solar cells.

Methods

Materials

All reagents and solvents were purchased and used without further purification. Formamidinium iodide (FAI, 99.9%), PbI_2 (99.99%), $PbBr_2$ (99.99%), PCBM (99.0%) and NiO_x (99.0%) nanoparticles were purchased from Advanced Election Technology. PDI (99.0%), methylammonium iodide (MAI, 99.0%), methylamine hydrochloride (>98.0%), Me-4PACz (>99.0%), CsI, guanidine thiocyanate (GuaSCN, >99.0) and BCP (>99.0) were obtained from TCI Japan. 1,4-Butanediamine (BDA, 98.0%) and NA (99.0%) were purchased from Aladdin. $PDAI_2$ (99.99%), 3MTPAI (99.99%), PEDOT:PSS aqueous solution (Al-4083), ethylenediammonium diiodide ($EDAI_2$, 99.99%), fullerene (C_{60}, 99.0%) and PI (99.0%) were purchased from Xi'an Yuri Solar. PEACl (99.0%) and PEAI (99.0%) were purchased from GreatCell Solar Materials. SnF_2 (99%), SnI_2 (99%), glycine hydrochloride (GlyHCl, 99.0%), KSCN (>99.0%) and Al_2O_3 (100 nm, 20 wt% in IPA) were purchased from Sigma-Aldrich. All solvents were purchased from Sigma-Aldrich with anhydrous grade.

Preparation of perovskite precursors and films

1.54-eV normal-bandgap perovskite for single-junction and mini-module PSCs. For the composition $Cs_{0.05}MA_{0.1}FA_{0.85}PbI_3$, a 1.8-M perovskite precursor solution was prepared by mixing CsI, MAI, FAI and PbI_2 in DMF:DMSO = 4:1, v/v mixed solvent subject to the stoichiometric ratio. An additional 9 mol% PbI_2 and 15 mol% methylamine hydrochloride were added to the precursor for better crystallization and perovskite phase transformation. The perovskite precursor (60 µl) was spin-coated on the substrate (dimensions 1.8 × 2.5 cm^2) at 5,000 r.p.m. for 50 s (5-s acceleration to 5,000 r.p.m.). 200 µl of chlorobenzene was dropped on the film 20 s before the end of the spinning program. The film was immediately annealed at 100 °C for 30 min.

1.68-eV-bandgap perovskite. For the composition $FA_{0.8}Cs_{0.2}Pb(I_{0.8}Br_{0.2})_3$, the precursor solution (1.5 M) was prepared by dissolving 1.2 mmol FAI, 0.3 mmol CsI, 1.05 mmol PbI_2, 0.45 mmol $PbBr_2$ and 0.03 mmol KSCN in mixed solvents of DMF and DMSO with a volume ratio of 3:1 and stirred overnight. The perovskite solution was spin-coated at 5,000 r.p.m. for 50 s (5-s acceleration to 5,000 r.p.m.), during which 200 µl of ethyl acetate was dropped on the film 20 s before the end of the spinning program. The film was subsequently annealed at 100 °C for 10 min.

1.77-eV WBG perovskite for all-perovskite tandem solar cells. For the composition $FA_{0.8}Cs_{0.2}Pb(I_{0.6}Br_{0.4})_3$, the precursor (1.2 M) was prepared by adding 0.96 mol FAI, 0.24 mmol CsI, 0.48 mmol PbI_2, 0.72 mmol $PbBr_2$ and 0.024 mmol KSCN to 1 ml DMF and DMSO mixed solvent (DMF:DMSO = 3:1, v/v). The spin-coating process was the same as that for the 1.68-eV-bandgap perovskite.

1.25-eV NBG perovskite for all-perovskite tandem solar cells. For the composition $Cs_{0.1}FA_{0.6}MA_{0.3}Sn_{0.5}Pb_{0.5}I_3$, the precursor (2.0 M) was prepared by mixing 0.2 mmol CsI, 1.2 mmol FAI, 0.6 mmol MAI, 1.0 mmol PbI_2, 1.0 mmol SnI_2, 0.1 mmol SnF_2, 0.04 mmol GlyHCl and 0.02 mmol GuaSCN into 1 ml mixed solvents of DMF and DMSO (DMF:DMSO = 3:1, v/v). The perovskite solution (60 µl) was spin-coated with the two-step spinning process (1,000 r.p.m. for 10 s and 4,000 r.p.m. for 40 s). Then, 300 µl of chlorobenzene was quickly dropped on the film during the second spin-coating step 20 s before the end of the procedure. The film was subsequently annealed at 100 °C for 10 min.

Small-area PSC fabrication

Single-junction normal-bandgap PSCs. ITO-coated glass substrates were cleaned thoroughly by sequential ultrasonication for 20 min in a detergent solution, ultrapure water, alcohol and IPA. Then, the substrates were dried with N_2 and cleaned with UV–ozone for 30 min before use. The NiO_x layer was formed by spin-coating NiO_x nanoparticle ink with a concentration of 5 mg ml^{-1} in a mixed solution of ultrapure water and IPA (H_2O:IPA = 3:1, v/v) onto the ITO substrate at 3,000 r.p.m. (3-s acceleration to 3,000 r.p.m.) for 20 s, then annealed at 110 °C for 10 min in the air and then transferred to an N_2-filled glovebox. Subsequently, solutions of Me-4PACz and NA with the same concentration (1 mmol l^{-1} in absolute ethanol) were mixed in a molar ratio of 3:1, and spin-coated on the NiO_x film at 3,000 r.p.m. for 20 s, followed by annealing at 100 °C for 10 min to form a mixed SAM layer. The 1.54-eV normal-bandgap perovskite solution was spin-coated on the NiO/SAM layer according to the aforementioned method. For the surface passivation, 4–6 mg of PDI was first dissolved in 3.6 ml of IPA, and then a minute quantity of NMP was added to the PDI-containing IPA to form the IPA-N (the supernatant of the supersaturated PDI solution was used for surface treatment) passivation strategy (NMP:IPA = 1:200, v/v), which was spin-coated on top of perovskite films (5,000 r.p.m., 30 s) and annealed at 100 °C for 3 min. Then, the PCBM solution (20 mg ml^{-1} in chlorobenzene) was spin-coated on the surface-passivated perovskite layer at 3,000 r.p.m. for 30 s, followed by annealing at 70 °C for 10 min. Sequentially, the saturated solution of BCP in methanol was dynamically spin-coated on the PCBM layer at 6,000 r.p.m. for 30 s and annealed at 70 °C for 10 min. The device was completed by thermal evaporation of Ag with a controlled evaporation rate of 0.1 Å s^{-1} to 0.5 Å s^{-1}, in a vacuum chamber (<5 × 10^{-4} Pa), to form the 120-nm Ag electrode. Specifically, we used a commercially available antireflective film (model GZ004) purchased from Zhoushan Huazhou Chemical Co. to reduce optical losses and enhance light coupling efficiency.

Single-junction NBG PSCs. The PEDOT:PSS solution was spin-coated on as-cleaned ITO substrates at 5,000 r.p.m. for 30 s and annealed on a hotplate at 150 °C for 20 min in ambient air. The samples (PEDOT:PSS-deposited ITO) were immediately transferred to an N_2-filled glovebox. The Al_2O_3-dispersed IPA solution was spin-coated onto the PEDOT:PSS layer at 6,000 r.p.m. for 20 s and annealed at 100 °C for 5 min. Then, the NBG perovskite solution was spin-coated according to the aforementioned method. For the surface passivation, the BDA-$EDAI_2$ layer was formed according to our previous work[39]. Then the sample was transferred to the vacuum evaporation system to deposit C_{60} (20-nm), BCP (7-nm) and Ag (120-nm) layers sequentially. The evaporation rates of C_{60} and BCP were controlled at around 0.2 Å s^{-1} and 0.1 Å s^{-1}, respectively.

Single-junction WBG PSCs. For the WBG PSCs, the whole preparation process was conducted in an N_2-filled glovebox. The Me-4PACz ethanol solution (0.8 mg ml^{-1}) was spin-coated on ITO substrates at 3,000 r.p.m. for 30 s and annealed for 10 min at 100 °C. Subsequently, the Al_2O_3 layer deposition, perovskite layer deposition and IPA-N surface passivation were conducted according to the aforementioned method. The deposition of C_{60}/BCP/Ag was the same as described for the NBG PSCs.

All-perovskite tandem devices. For the WBG subcell, the Me-4PACz, Al_2O_3, 1.77-eV WBG perovskite, IPA-N and C_{60} were sequentially deposited using the same procedure as for single-junction WBG PSCs. Then, to make the tunnel recombination junction, the SnO_x (30-nm)/

Au (1-nm) layer was deposited on the WBG perovskite layer using atomic layer deposition (ALD) for SnO_x and a thermal evaporation system for Au. The SnO_x films were deposited via ALD at 100 °C, using tetrakis(dimethylamino)tin (TDMASn) and H_2O as precursors. The TDMASn precursor was heated to 70 °C, while the water source was kept at room temperature. N_2 was used as the purge gas, with flow rates of 7.5 sccm for the heated TDMASn precursor and 7.0 sccm for the room-temperature water precursor. One complete ALD cycle consisted of a 0.08-s TDMASn dose, a 6-s nitrogen purge, a 0.025-s water dose and another 6-s nitrogen purge. The deposition rate was approximately 0.12 nm per cycle. After this, the PEDOT:PSS/IPA (1:2, v/v) solution was spin-coated at 4,000 r.p.m. for 30 s and annealed at 100 °C for 15 min in ambient air. Then the sample was transferred to an N_2-filled glovebox, and perovskite films, BDA-$EDAI_2$, C_{60}, BCP and Ag electrodes were prepared using the same procedure as for the NBG PSCs. Finally, we successively fabricate all-perovskite tandem solar cells with the architecture glass/ITO/Me-4PACz/WBG perovskite/IPA-N/C_{60}/ALD-SnO_x (30 nm)/Au (1 nm)/PEDOT:PSS/NBG perovskite/BDA-$EDAI_2$/C_{60}/BCP/Ag.

Single-junction 1.68-eV-bandgap PSCs. The preparation process was the same as that of the single-junction WBG PSCs.

Mini-module fabrication. The mini-modules were fabricated on 5-cm × 5-cm glass/fluorine-doped tin oxide substrates. After cleaning, P1 scribing was performed using a 532-nm, 2-W nanosecond laser to isolate subcells. The substrates were dried with nitrogen and treated with UV–ozone for 30 min. A perovskite precursor solution (300 µl) was spin-coated at 5,000 r.p.m. for 50 s (5-s ramp), with 500 µl of chlorobenzene dropped 20 s before the end. Following BCP deposition, P2 and P3 scribing were conducted using a 0.3-W laser to pattern the functional layers and Ag electrode (100 nm), respectively. An additional P4 scribe, using the same laser settings as P1, was applied to clean the module edges. Each module consisted of five subcells (6.8-mm width), achieving a geometric fill factor of ~97.5% and an aperture area of 11.1 cm^2.

Stability tests

The device encapsulation was carried out according to our previous report[40,41]. The Bi/Cu (20-nm/120-nm) bilayer electrode was used instead of the Ag electrode for stability tests[42]. The devices were first encapsulated by ALD of approximately 20-nm-thick Al_2O_3 films. Subsequently, a layer of POE (polyolefin elastomer) film was applied on top of the ALD-covered area, leaving a small region at the electrodes for soldering tinned copper ribbons to extend the electrical connections. The devices were then covered with a glass plate, with the edges sealed using 1-cm-wide butyl tape. Finally, the encapsulated devices were vacuum laminated at 120 °C for 20 min using an industrial laminator to complete the final encapsulation. The operational stability of the encapsulated devices was conducted using a commercial multichannel stability test system (Wuhan 91PVKSolar) according to our previous work. A quantitative analysis of the LED spectrum in Supplementary Fig. 52 revealed that 32.4% of the total irradiance lies in the wavelength region below 550 nm, which is highly consistent with the corresponding value in the standard AM1.5G spectrum (33.35%). This indicates that the LED provides sufficient light intensity in the UV and blue regions. This indicates that the LED provides sufficient light intensity in the UV and blue regions. For the 85 °C thermal stability test, the unencapsulated devices were placed on a hotplate at 85 °C in an N_2-filled glovebox, and the *J*–*V* curves were measured periodically after the devices cooled to room temperature.

Characterization

The steady-state PL spectra were recorded using a home-built set-up utilizing the ProSp-Micro-MVIS microspectroscopy system (Hangzhou SPL Photonics Co.) The samples were excited with a 405-nm laser, and the data were collected using a QE-Pro monochromator from Ocean Optics. ^{1}H nuclear magnetic resonance spectra were recorded at room temperature using a 600-MHz Bruker AVANCE III-600 nuclear magnetic resonance spectrometer. The samples were dissolved in deuterated DMSO (DMSO-d_6). The top-view and cross-sectional images of the samples were obtained using a field-emission scanning electron microscope (FEI NOVA NanoSEM 450). UV–vis absorption spectra were obtained using a UV–vis spectrometer (PerkinElmer). In situ GIWAXS characterizations were performed at BL14B and 20U2 RSoXS beamlines at the Shanghai Synchrotron Facility and BL17B1 beamline at the National Facility for Protein Science in Shanghai, China. The incidence angles were 0.2° and 0.8°. In situ PL spectra were recorded on a Du-100 dynamic spectrometer system (Puguangweishi Co.) in an N_2-filled glovebox, and a 375-nm laser with a maximum power of 30 W was used as the excitation source. The grazing-incidence X-ray diffraction patterns were acquired in air by using a Rigaku SmartLab with Cu Kα radiation in the 2θ range from 30.6° to 32.6°. The time-resolved PL spectra were measured using a time-correlated single-photon counting system, with a pulsed laser source of 410-nm wavelength and a repetition rate of 5 MHz. To ensure low injection conditions and avoid nonlinear effects, the laser fluence is 15.8 nJ cm^{-2}, and the power density was controlled to be below 0.0016 W cm^{-2} during the measurements, with a pulse duration of approximately 80 ps. The carrier lifetime was fitted using a biexponential decay equation of $y = A_1 \exp(-t/\tau_1) + A_2 \exp(-t/\tau_2) + y_0$. Fluorescence lifetime imaging microscopy was carried out using a FLIM300 (Dalian Chuangrui Spectrum). The ultraviolet photoelectron spectroscopy data were obtained using an AXIS-ULTRA DLD-600 W Ultra spectrometer (Kratos) equipped with a non-monochromatic He Iα photon source ($h\nu$ = 21.22 eV). An X-ray photoelectron spectroscopy system (Thermo ESCALAB 250XI) equipped with a monochromatic Al Kα X-ray source (1,486.6 eV) operating at 100 W was used to acquire the X-ray photoelectron spectra). Atomic-force-microscopy-based infrared spectroscopy experiments were conducted using a Bruker Nano-IR_3 at wavenumbers ranging from 1,600 to 1,800 cm^{-1}. The trap density of states was estimated from thermal admittance spectroscopy measurements based on the method reported elsewhere. Ultrafast transient absorption spectroscopy was carried out using a Helios spectrometer (Ultrafast Systems), with a pump source provided by a Ti:sapphire regenerative amplifier (Legend Elite, Coherent) operating at a repetition rate of 5 kHz, with a fundamental wavelength of 800 nm and a pulse width of approximately 40 fs. The excitation wavelength of 520 nm was generated via a TOPAS optical parametric amplifier, and the excitation power was set to 0.3 µW with a pump spot diameter of approximately 100 µm. On the basis of these excitation parameters, we estimated the photon fluence to be $F \approx 0.038$ µJ cm^{-2}. Taking into account the absorption characteristics of the film and assuming that each photon generates one electron–hole pair, the estimated carrier density per pulse is of the order of 10^{16} cm^{-3}, which corresponds to a relatively high-injection regime. This condition ensures that the measurements were performed within the linear response region, thereby minimizing the influence of nonlinear effects on the kinetic analysis. Moreover, to enhance transmission and improve the signal-to-noise ratio, we employed a diluted perovskite precursor solution with a concentration of 0.75 M for film fabrication. The probe beam (white-light continuum) was generated by focusing on an yttrium aluminium garnet plate. The pump and probe beams were spatially overlapped on the sample at a small angle of less than 10°. A linear CCD (charge-coupled device) array collected the transmitted probe light from the sample. The transient absorption spectra at selected pump–probe delay time were fitted by biexponential decay. The *J*-*V* curves of the devices were recorded with a black mask with an active area of 0.05556 cm^2 using a Keithley 2400 SourceMeter and a solar simulator (Oriel, model 9119) under AM1.5G 1-sun illumination. The light intensity was adjusted with a reference silicon solar cell (KG3, Enlitech). During the *J*-*V* measurement, a voltage scanning speed of 100 mV s^{-1} and a voltage step size

of ~0.02 V were applied for both forward and reverse voltage scanning directions. The EQE spectra were measured under direct-current mode using an EQE system (Saifan) with monochromatic light of 1×10^{16} photons cm^{-2}. The transient photocurrent measurements and *C*–*V* curves were obtained using a Zennium electrochemistry workstation (Zahner). The PLQY of the corresponding film was measured using a QuantaMaster 8000 (HORIBA, Canada) with a 405-nm laser to photoexcite the samples placed in an integrating sphere. The laser's intensity was calibrated by adjusting the power when it produced a 1-sun-equivalent current density from the devices under J_{SC} conditions.

DFT calculations

All DFT calculations were performed with the Vienna Ab Initio Simulation Package (VASP 5.4.4) and Gaussian 09 (G09) program package for periodic and molecular systems, respectively[43–47]. In the VASP calculation, the projector augmented wave method[46–49] was employed, and exchange–correlation interactions were treated through the Perdew–Burke–Ernzerhof[50] functional under the generalized gradient approximation. Integration in the Brillouin zone was performed on the basis of the Monkhorst–Pack scheme using $2 \times 2 \times 1$ *k*-point meshes in each primitive lattice vector of the reciprocal space for geometry optimization of $FAPbI_3$ surface structures incorporated with PDI and solvents (NMP and IPA)[51]. We used the DFT-D3 dispersion correction method to reflect the non-bonding interaction correlation in the perovskite structure[50,52]. Lattice constants and internal atomic positions were fully optimized using a plane-wave cutoff energy of 500 eV until the residual forces were less than 0.04 eV $Å^{-1}$. To examine the surface properties of $FAPbI_3$ for PDI binding, we designed surface models of $FAPbI_3$ with a 15-Å vacuum gap in the *z* direction, which prevented interlayer interactions, and the bottom two layers were fixed to represent their bulk properties.

The binding energy (ΔE_b) of PDI to the $FAPbI_3$ surface structure was calculated using following equation: $\Delta E_b = (E^{PDI}_{FAPbI_3} - E_{FAPbI_3} - E_{PDI})$, where $E^{PDI}_{FAPbI_3}$ is the total energy of the fully relaxed $FAPbI_3$ surface structure with PDI, E_{FAPbI_3} is the total energy of the $FAPbI_3$ surface structure and E_{PDI} is the total energy of PDI. In addition, the molecular ΔE_{int} of PDI and solvents (NMP and IPA) was calculated using following equation: $\Delta E_{int} = E^{PDI}_{solvent} - E_{PDI} - E_{solvent}$, where $E^{PDI}_{solvent}$ is the total energy of PDI-bound NMP and IPA molecular structures and E_{PDI} and $E_{solvent}$ are the total energies of PDI and NMP/IPA, respectively. For molecular systems, calculations were performed using G09 at the B3LYP/6-31G* level. The energy minima were confirmed by verifying the absence of imaginary vibrational modes, and Mulliken charge analysis was conducted[53].

Reporting summary

Further information on research design is available in the Nature Portfolio Reporting Summary linked to this article.

Data availability

The data that support the findings of this study are available within the Article and its Supplementary Information. Source data are provided with this paper.

References

1. Kim, H.-S. et al. Lead iodide perovskite sensitized all-solid-state submicron thin film mesoscopic solar cell with efficiency exceeding 9%. *Sci. Rep.* **2**, 591 (2012).
2. Yang, W. S. et al. High-performance photovoltaic perovskite layers fabricated through intramolecular exchange. *Science* **348**, 1234–1237 (2015).
3. Liu, S., Biju, V. P., Qi, Y., Chen, W. & Liu, Z. Recent progress in the development of high-efficiency inverted perovskite solar cells. *NPG Asia Mater.* **15**, 27 (2023).
4. Liu, C. et al. Bimolecularly passivated interface enables efficient and stable inverted perovskite solar cells. *Science* **382**, 810–815 (2023).
5. Liu, S. et al. Buried interface molecular hybrid for inverted perovskite solar cells. *Nature* **632**, 536–542 (2024).
6. Zheng, Y. et al. Towards 26% efficiency in inverted perovskite solar cells via interfacial flipped band bending and suppressed deep-level traps. *Energy Environ. Sci.* **17**, 1153–1162 (2024).
7. Yang, Y. et al. Amidination of ligands for chemical and field-effect passivation stabilizes perovskite solar cells. *Science* **386**, 898–902 (2024).
8. Zhang, S. et al. Minimizing buried interfacial defects for efficient inverted perovskite solar cells. *Science* **380**, 404–409 (2023).
9. Li, Z. et al. Stabilized hole-selective layer for high-performance inverted p–i–n perovskite solar cells. *Science* **382**, 284–289 (2023).
10. Qu, G. et al. Conjugated linker-boosted self-assembled monolayer molecule for inverted solar cells. *Joule* **8**, 2123–2134 (2024).
11. Park, S. M. et al. Engineering ligand reactivity enables high-temperature operation of stable perovskite solar cells. *Science* **381**, 209–215 (2023).
12. Li, F. et al. Regulating surface termination for efficient inverted perovskite solar cells with greater than 23% efficiency. *J. Am. Chem. Soc.* **142**, 20134–20142 (2020).
13. Jiang, Q. et al. Surface reaction for efficient and stable inverted perovskite solar cells. *Nature* **611**, 278–283 (2022).
14. Xiong, S. et al. Reducing nonradiative recombination for highly efficient inverted perovskite solar cells via a synergistic bimolecular interface. *Nat. Commun.* **15**, 5607 (2024).
15. Zhu, H. et al. In situ energetics modulation enables high-efficiency and stable inverted perovskite solar cells. *Nat. Photon.* **19**, 28–35 (2024).
16. Duan, T. et al. Chiral-structured heterointerfaces enable durable perovskite solar cells. *Science* **384**, 878–884 (2024).
17. Zang, X. et al. Passivating dipole layer bridged 3D/2D perovskite heterojunction for highly efficient and stable p–i–n solar cells. *Adv. Mater.* **36**, 2309991 (2024).
18. Teale, S., Degani, M., Chen, B., Sargent, E. H. & Grancini, G. Molecular cation and low-dimensional perovskite surface passivation in perovskite solar cells. *Nat. Energy* **9**, 779–792 (2024).
19. Xiao, Y., Yang, X., Zhu, R. & Snaith, H. J. Unlocking interfaces in photovoltaics. *Science* **384**, 846–848 (2024).
20. Chen, H. et al. Quantum-size-tuned heterostructures enable efficient and stable inverted perovskite solar cells. *Nat. Photon.* **16**, 352–358 (2022).
21. Wang, M. et al. Ammonium cations with high pK_a in perovskite solar cells for improved high-temperature photostability. *Nat. Energy* **8**, 1229–1239 (2023).
22. Jiang, Q. et al. Surface passivation of perovskite film for efficient solar cells. *Nat. Photon.* **13**, 460–466 (2019).
23. Yu, S. et al. Homogenized NiO_x nanoparticles for improved hole transport in inverted perovskite solar cells. *Science* **382**, 1399–1404 (2023).
24. Li, X. et al. Surface reconstruction for efficient and stable monolithic perovskite/silicon tandem solar cells with greatly suppressed residual strain. *Adv. Mater.* **35**, 2211962 (2023).
25. Wang, H. et al. Pre-annealing treatment for high-efficiency perovskite solar cells via sequential deposition. *Joule* **6**, 2869–2884 (2022).

26. Huang, X. et al. Solvent gaming chemistry to control the quality of halide perovskite thin films for photovoltaics. *ACS Cent. Sci.* **8**, 1008–1016 (2022).
27. Steele, J. A. et al. How to GIWAXS: grazing incidence wide angle x-ray scattering applied to metal halide perovskite thin films. *Adv. Energy Mater.* **13**, 2300760 (2023).
28. Wang, S. et al. In situ self-elimination of defects via controlled perovskite crystallization dynamics for high-performance solar cells. *Adv. Mater.* **35**, 2305314 (2023).
29. Lin, Y.-H. et al. Bandgap-universal passivation enables stable perovskite solar cells with low photovoltage loss. *Science* **384**, 767–775 (2024).
30. Huang, Z. et al. Anion–π interactions suppress phase impurities in $FAPbI_3$ solar cells. *Nature* **623**, 531–537 (2023).
31. Liang, Z. et al. Homogenizing out-of-plane cation composition in perovskite solar cells. *Nature* **624**, 557–563 (2023).
32. Meng, H. et al. Inhibition of halide oxidation and deprotonation of organic cations with dimethylammonium formate for air-processed p–i–n perovskite solar cells. *Nat. Energy* **9**, 536–547 (2024).
33. Liu, H. et al. Surface formamidine cation immobilization for efficient FA-based perovskites solar cells. *Adv. Energy Mater.* **14**, 2401809 (2024).
34. Wang, T. et al. Dimensional regulation from 1D/3D to 2D/3D of perovskite interfaces for stable inverted perovskite solar cells. *J. Am. Chem. Soc.* **146**, 7555–7564 (2024).
35. Hieulle, J. et al. Understanding and decoupling the role of wavelength and defects in light-induced degradation of metal-halide perovskites. *Energy Environ. Sci.* **17**, 284–295 (2024).
36. Park, S. M. et al. Low-loss contacts on textured substrates for inverted perovskite solar cells. *Nature* **624**, 289–294 (2023).
37. Chen, S., Xiao, X., Gu, H. & Huang, J. Iodine reduction for reproducible and high-performance perovskite solar cells and modules. *Sci. Adv.* **7**, eabe813 (2021).
38. Chu, X. et al. Surface in situ reconstruction of inorganic perovskite films enabling long carrier lifetimes and solar cells with 21% efficiency. *Nat. Energy* **8**, 372–380 (2023).
39. Pan, Y. et al. Surface chemical polishing and passivation minimize non-radiative recombination for all-perovskite tandem solar cells. *Nat. Commun.* **15**, 7335 (2024).
40. Chen, R. et al. Reduction of bulk and surface defects in inverted methylammonium- and bromide-free formamidinium perovskite solar cells. *Nat. Energy* **8**, 839–849 (2023).
41. Zhou, J. et al. Modulation of perovskite degradation with multiple-barrier for light-heat stable perovskite solar cells. *Nat. Commun.* **14**, 6120 (2023).
42. Wu, S. et al. A chemically inert bismuth interlayer enhances long-term stability of inverted perovskite solar cells. *Nat. Commun.* **10**, 1161 (2019).
43. Frisch, M. et al. *Gaussian 09* (Gaussian Inc., 2009).
44. Kresse, G. & Hafner, J. Ab initio molecular dynamics for open-shell transition metals. *Phys. Rev. B* **48**, 13115–13118 (1993).
45. Kresse, G. & Hafner, J. Ab initio molecular-dynamics simulation of the liquid-metal–amorphous-semiconductor transition in germanium. *Phys. Rev. B* **49**, 14251–14269 (1994).
46. Kresse, G. & Furthmüller, J. Efficiency of ab-initio total energy calculations for metals and semiconductors using a plane-wave basis set. *Comput. Mater. Sci.* **6**, 15–50 (1996).
47. Kresse, G. & Furthmuller, J. Efficient iterative schemes for ab initio total-energy calculations using a plane-wave basis set. *Phys. Rev. B* **54**, 11169–11186 (1996).
48. Blöchl, P. E. Projector augmented-wave method. *Phys. Rev. B* **50**, 17953–17979 (1994).
49. Kresse, G. & Joubert, D. From ultrasoft pseudopotentials to the projector augmented-wave method. *Phys. Rev. B* **59**, 1758–1775 (1999).
50. Perdew, J. P., Burke, K. & Ernzerhof, M. Generalized gradient approximation made simple. *Phys. Rev. Lett.* **77**, 3865–3868 (1996).
51. Monkhorst, H. J. & Pack, J. D. Special points for Brillouin-zone integrations. *Phys. Rev. B* **13**, 5188–5192 (1976).
52. Grimme, S., Antony, J., Ehrlich, S. & Krieg, H. A consistent and accurate ab initio parametrization of density functional dispersion correction (DFT-D) for the 94 elements H–Pu. *J. Chem. Phys.* **132**, 154104 (2010).
53. Modelli, A., Mussoni, L. & Fabbri, D. Electron affinities of polycyclic aromatic hydrocarbons by means of B3LYP/6-31+G* calculations. *J. Phys. Chem. A* **110**, 6482–6486 (2006).
54. Chen, H. et al. Improved charge extraction in inverted perovskite solar cells with dual-site-binding ligands. *Science* **384**, 189–193 (2024).
55. Tan, Q. et al. Inverted perovskite solar cells using dimethylacridine-based dopants. *Nature* **620**, 545–551 (2023).

Acknowledgements

We thank the Analytical and Testing Center of Huazhong University of Science and Technology for their support in sample measurements. We thank the staff members of BL14B and 20U2 RSoXS beamlines at the Shanghai Synchrotron Facility and BL17B1 beamlines at the National Facility for Protein Science in Shanghai for technical support in the collection and analysis of X-ray diffraction data. We thank the Center for Computational Science and Engineering at Southern University of Science for providing the computing resources. Funding: N.-G.P. thanks the National Research Foundation of Korea (NRF) for grants funded by the Korean government (MSIT) under contract NRF-2021R1A3B1076723 (Research Leader Program), NRF-2022M3J1A1085280 (Carbon Neutral Technology Program) and RS-2023-00259096 (GRDC Cooperative Hub). W.C. acknowledges financial support from the National Key Research and Development Project funding from the Ministry of Science and Technology of China (2021YFB3800104), the National Natural Science Foundation of China (W2412077, U20A20252) and the Innovation Project of Optics Valley Laboratory (OVL2021BG008). Z.L. acknowledges the National Natural Science Foundation of China (52473301), the Young Elite Scientists Sponsorship Program by CAST, the Natural Science Foundation of Hubei Province (2022CFA093) and the Self-Determined and Innovative Research Funds of HUST (2020kfyXJJS008), the Fundamental Research Support Program of Huazhong University of Science and Technology (2025BRB016) and the State Key Laboratory of Alternate Electrical Power System with Renewable Energy Sources (LAPS25001).

Author contributions

S.L., T.M., J.W., Y.Z. and R.C. contributed equally to this work. N.-G.P., W.C., Z.L. and S.L. conceived the project. S.L., T.M., J.W. and R.C. fabricated devices. S.L., T.M., J.W., Y.Z., R.C., E.X. and Y.S. carried out the material and device characterizations. W.Q., Z.Z., L. Lu and Z.C. carried out the in situ GIWAXS measurements. P.C., L. Li and M.L. conducted the in situ PL measurements. X.L. performed the DFT calculations under the supervision of Y.Z. S.C.C. performed the DFT calculations under the supervision of S.U.L. S.-H.C. investigated the effect of IPA-N for data reproducibility. T.M., J.W., Y.Z. and R.C provided useful suggestions for the paper. S.L., T.M., J.W., Y.Z., R.C., Z.L., W.C. and N.-G.P. analysed all experimental data. S.L., T.M., J.W., Y.Z. and R.C. prepared the manuscript under the supervision of Z.L., W.C. and N.-G.P.

Competing interests

The authors declare no competing interests.

Additional information

Supplementary information The online version contains supplementary material available at https://doi.org/10.1038/s41560-025-01912-8.

Correspondence and requests for materials should be addressed to Zonghao Liu, Wei Chen or Nam-Gyu Park.

Peer review information *Nature Energy* thanks the anonymous reviewer(s) for their contribution to the peer review of this work.

nature portfolio

Corresponding author(s): Nam-Gyu Park

Solar Cells Reporting Summary

Nature Portfolio wishes to improve the reproducibility of the work that we publish. This form is intended for publication with all accepted papers reporting the characterization of photovoltaic devices and provides structure for consistency and transparency in reporting. Some list items might not apply to an individual manuscript, but all fields must be completed for clarity.

For further information on Nature Research policies, including our data availability policy, see Authors & Referees.

Experimental design

Please check the following details are reported in the manuscript, and provide a brief description or explanation where applicable.

1. Dimensions

Area of the tested solar cells	☒ Yes	Aperture areas of 0.0496, 0.05556 and 11.09 cm2 were used in this work.
	☐ No	*Explain why this information is not reported/not relevant.*
Method used to determine the device area	☒ Yes	The active area was determined by the aperture shade ma placed in front of the solar cell
	☐ No	*Explain why this information is not reported/not relevant.*

2. Current-voltage characterization

Current density-voltage (J-V) plots in both forward and backward direction	☒ Yes	Fig. 4a
	☐ No	
Voltage scan conditions	☒ Yes	The J–V curves of the single-junction devices were recorded with a black mask with an active area of 0.05556 cm2 using a Keithley 2400 SourceMeter and a solar simulator (Oriel, model 9119) under AM 1.5G one sun illumination. The light intensity was adjusted with a reference silicon solar cell (KG3, Enlitech). The scanning speed for both forward (-0.1 V〜1.22 V) and reverse scans (1.22 V〜-0.1V) was 0.02 V s−1.
	☐ No	*Explain why this information is not reported/not relevant.*
Test environment	☒ Yes	Supplementary Fig. 41: Sample temperature: 25±2 °C, irradiance: 1000 W/m2, standard solar spectral irradiance distribution corresponding to IEC60904-3.
	☐ No	*Explain why this information is not reported/not relevant.*
Protocol for preconditioning of the device before its characterization	☐ Yes	*Provide a description of the protocol.*
	☒ No	No preconditioning is needed
Stability of the J-V characteristic	☒ Yes	Supplementary Fig. 41: Sample temperature: 25±2 °C, irradiance: 1000 W/m2, standard solar spectral irradiance distribution corresponding to IEC60904-3, continuously scan the maximum power point (Pmax) of sample for 5 minutes. Take the average Pmax of last 5 minutes. The stabilized PCE of 26.87% (Average Pmax=1.493 mW)determined from MPPT for 300 s.
	☐ No	*Explain why this information is not reported/not relevant.*

3. Hysteresis or any other unusual behaviour

Description of the unusual behaviour observed during the characterization	☐ Yes	*Provide a description of hysteresis or any other unusual behaviour observed during the characterization.*
	☒ No	low hysteresis was observed both for single-junction and tandem devices.
Related experimental data	☒ Yes	J-V curves under reverse and forward scans were provided in Fig. 4a and 4e. For the single-junction devices, the power conversion efficiencies (PCEs) under forward and reverse scans are 26.99% and 27.19%, respectively. For the tandem devices, the corresponding PCEs are 28.96% and 29.27%
	☐ No	*Explain why this information is not reported/not relevant.*

4. Efficiency

External quantum efficiency (EQE) or incident photons to current efficiency (IPCE)

☒ Yes
☐ No

Supplementary Fig. 39. The integrated JSC of the champion inverted PSC form EQE curve is 25.61 mA/cm2

Explain why this information is not reported/not relevant.

A comparison between the integrated response under the standard reference spectrum and the response measure under the simulator

☒ Yes
☐ No

The integrated Jsc values obtained from EQE were agree well with the Jsc determined from J-V curve.

Explain why this information is not reported/not relevant.

For tandem solar cells, the bias illumination and bias voltage used for each subcell

☒ Yes
☐ No

Supplementary Fig. 59: AAA Steady State Solar Simulator (YSS-T155-2M); Logarithmic sweep in both directions (Voc to Isc (2.2 V〜-0.1 V) and Isc to Voc (-0.1 V〜-2.2 V)) based on IEC60904-1:200.

Explain why this information is not reported/not relevant.

5. Calibration

Light source and reference cell or sensor used for the characterization

☒ Yes
☐ No

A solar simulator (Oriel, model 9119) with an AM1.5G spectrum in the lab.The light intensity was calibrated with a reference silicon solar cell (KG-3,KG-5,KG-0 Enlitech).

Explain why this information is not reported/not relevant.

Confirmation that the reference cell was calibrated and certified

☒ Yes
☐ No

The light intensity was calibrated by the reference solar cell (SCI-REF-Q) from Sciencetech for certification.

Explain why this information is not reported/not relevant.

Calculation of spectral mismatch between the reference cell and the devices under test

☐ Yes
☒ No

Provide a value of the spectral mismatch and/or a description of how it has been taken into account in the measurements.

We rely on certified efficiency results

6. Mask/aperture

Size of the mask/aperture used during testing

☒ Yes
☐ No

Metal aperture masks with areas of 0.0556 (single-junction devices), 0.0496 (tandem devices), and 11.09 cm2 (mini-modules) were used for testing.

Explain why this information is not reported/not relevant.

Variation of the measured short-circuit current density with the mask/aperture area

☐ Yes
☒ No

Report the difference in the short-circuit current density values measured with the mask and aperture area.

All J-V curves were measured with a metal aperture mask

7. Performance certification

Identity of the independent certification laboratory that confirmed the photovoltaic performance

☒ Yes
☐ No

Small-area PSC: Chinese National Center of Inspection on Solar Photovoltaic Products Quality; Tandem device: Shanghai Institute of Microsystem and Information Technology (SIMIT); Mini-module: Hangzhou branch of TÜV Rheinland Group, Germany

Explain why this information is not reported/not relevant.

A copy of any certificate(s)

☒ Yes
☐ No

Supplementary Fig. 41, 47 and 59

Explain why this information is not reported/not relevant.

8. Statistics

Number of solar cells tested

☒ Yes
☐ No

Supplementary Fig. 37: collected from 20 cells for each condition

Explain why this information is not reported/not relevant.

Statistical analysis of the device performance

☒ Yes
☐ No

Supplementary Table 5 presents the statistical analysis corresponding to Supplementary Fig. 37.

Explain why this information is not reported/not relevant.

9. Long-term stability analysis

Type of analysis, bias conditions and environmental conditions

☒ Yes
☐ No

Operational stability of encapsulated single junction devices under continuous 1-sun-equivalent white-light LED illumination at 65 °C with maximum power point tracking in ambient air. The initial PCEs of the representative control and IPA-N devices used for the operational stability test were 24.27% and 26.12%, respectively. A quantitative analysis of the LED spectrum in Supplementary Fig. 52 revealed that 32.4% of the total irradiance lies in the wavelength region below 550 nm, which is highly consistent with the corresponding value in the standard AM1.5G spectrum (33.35%). This indicates that the LED provides sufficient light intensity in the UV and blue regions

Explain why this information is not reported/not relevant.